Quantifying Firebrand Production and Transport Using the Acoustic Analysis of In-Fire Cameras

Dan K. Thompson ⬡*, Canadian Forest Service, Great Lakes Forestry Centre, Natural Resources Canada, Sault Ste. Marie, Canada*

Daniel A. Yip, Wildlife Conservation Society Canada, Whitehorse, Canada

Eunmo Koo and Rod Linn, Los Alamos National Laboratory, Los Alamos, USA

Ginny Marshall, Canadian Forest Service, Natural Resources Canada, Northern Forestry Centre, Edmonton, Canada

Razim Refai, FPInnovations Wildfire Operations Research, Edmonton, Canada

Dave Schroeder, Wildfire Management Branch, Alberta Agriculture and Forestry, Edmonton, Canada

Abstract. Firebrand travel and ignition of spot fires is a major concern in the Wildland-Urban Interface and in wildfire operations overall. Firebrands allow for the efficient breaching across fuel-free barriers such as roads, rivers and constructed fuel breaks. Existing observation-based knowledge on medium-distance firebrand travel is often based on single tree experiments that do not replicate the intensity and convective updraft of a continuous crown fire. Recent advances in acoustic analysis, specifically pattern detection, has enabled the quantification of the rate at which firebrands are observed in the audio recordings of in-fire cameras housed within fire-proof steel boxes that have been deployed on experimental fires. The audio pattern being detected is the sound created by a flying firebrand hitting the steel box of the camera. This technique allows for the number of firebrands per second to be quantified and can be related to the fire's location at that same time interval (using a detailed rate of spread reconstruction) in order to determine the firebrand travel distance. A proof of concept is given for an experimental crown fire that shows the viability of this technique. When related to the fire's location, key areas of medium-distance spotting are observed that correspond to regions of peak fire intensity. Trends on the number of firebrands landing per square metre as the fire approaches are readily quantified using low-cost instrumentation.

*Correspondence should be addressed to: Dan K. Thompson, E-mail: Daniel.thompson@canada.ca

1. Introduction

Firebrands have been recognized as the primary vector for wildfire home ignition over direct flame contact [1] due to the ability of firebrands to reach fine fuels (e.g. leaf debris on a roof) not otherwise exposed to radiative heating from flames. In wildfire spread, spot fires due to firebrand travel and ignition ahead of the main fire front have been recorded at distances upwards of 4 km [2]. In fire environments with numerous fuel-free areas (i.e. rocky outcrops in mountains or lakes in northern circumboreal forest), firebrands offer an efficient vector for spread in discontinuous fuels. For suppression operations, an understanding of the expected rate of firebrand breaching across roadways or constructed mechanical fire guard (i.e. mechanically cleared swaths) is important for forecasting crew resource demand to extinguish small spot fires from firebrand travel across linear features.

Four distinct physical processes relevant to firebrands were defined by Koo et al. [3]: firebrand generation, transport, deposition and ignition, followed by surface fire spread. The initiation of surface fire spread in forest fuels is a generally well-understood phenomenon, stemming from extensive field testing of simple empirical models of point ignition and sustained flaming [4]. Firebrand transport has been the subject of laboratory and numerical studies for decades [5], resulting in a series of increasingly applied [6, 7] and complex [3] firebrand transport models to suit a variety of user needs. Of the key firebrand processes, the generation of firebrands was highlighted as a key uncertainty in a recent review by [8]. Specifically, the need for additional methodologies to observe firebrand generation under realistic heat release rate and fuel conditions was cited as a key gap in the understanding of firebrands.

Most observational studies of firebrand production and transport are from stationary fires, such as structure fires ([9–13]) which are often used to inform models of fire spread within urban areas under high winds [14] where firebrands are an important vector for structure-to-structure ignition, above and beyond the classical radiant and convective heat transfer from flames [10]. Stationary experimental fires, while an important source of information on firebrand production and transport, do not fully replicate the environmental conditions of a free-burning crown fire in conifer forest, where the rapid consumption of primarily fine canopy fuels (fine brachwood and foliage) alongside surface litter [15] provide a contrasting fuel composition compared to more thermally thick building materials [9, 12]. Furthermore, the interaction of a wind-driven elongated fire front with the atmosphere introduces complexities for fire spread [16] that may have implications for firebrand transport compared to point-source stationary fires. Similarly, laboratory methods of firebrand production provide extremely valuable insights on structure ignition processes, but the impact of mitigation measures such as forest fuel reduction on firebrand production and transport in conifer crown fires remain largely limited to physics-based modelling [17].

Recent experiments to measure firebrand production in a wind tunnel setting [20] do not capture the turbulent convection of a high-intensity crown fire where firebrand transport is greatest and most important to landscape-scale fire spread [21]. Firebrand production factors are essential input for fire physics models that

can simulate the turbulence around firebrands (i.e. [3]). Data is typically challenging to acquire at the head of crown fires when utilizing incidental materials [22] or purpose-built water collection pans [23]. Similarly, studies utilizing aerial infrared imagery of active fires to identify spot fires ahead of the main fire front [2, 24] quantify only those firebrands able to immediately ignite and accelerate to a new sizable fire, but may not capture firebrands with lesser energy that may be important in structure ignitions [25] or new ignitions on the forest floor. 3D particle tracking velocimetry had been shown as a powerful instrument to track firebrand count and other relevant metrics [26], but multiple deployments of such instruments would be challenging ahead of and within a crown fire. Simple and robust instrumentation for experimental crown fires is necessary for further data collection of firebrand production and transport processes in addition to the established and valuable methods above.

In-fire cameras have been used since the 1990s [27] alongside other instrumentation such as thermocouples to examine fire behaviour during the passage of high-intensity boreal crown fires [28] in large experimental conifer crown fires, each multiple hectares in size. Such large experimental fires mimic the realistic fuel, weather, and heat release rate conditions of wildfires, but also benefit from the pre-placement of instrumentation. Though expensive to conduct and infrequently achieved, these large experimental fires provide a partial solution to the tension between laboratory and incident (real world) studies as highlighted in [8].

During experimental fires such as [28], cameras are typically contained within insulated steel boxes and placed on tripods 1.0–1.5 m above the ground, facing the direction of fire spread. While the audio track has been recorded and archived as incidental information, the information contained in the audio such as the sound of firebrands impacting the camera box has not previously been quantified. Acoustic impulsive events, the autogenic production of sound from the combustion process itself, has been documented in laboratory ignitions of conifer seedlings [29], though for microphones placed approximately 0.25 m from a low-intensity flame. In contrast, firebrands that drive medium-distance structure ignition, spot fire production, and enhancing fire spread travel on the order of 30 m [22] to upwards of a kilometre [24]. In this study, we demonstrate the novel application of in-fire camera sound recordings paired with detailed rate of spread information to yield time and distance information of firebrand landing rates during an experimental boreal crown fire. Importantly, while this method may have some drawbacks compared to firebrand-specific collection instruments, the methodology presented here requires no new instrumentation, and is compatible with archival in-fire footage during high-intensity crown fire.

Recent advances in acoustic pattern recognition in the field of bioacoustics and soundscape ecology have greatly increased our ability to automate the identification of target signals or patterns in large volumes of data [30]. Automated recognition has successfully been used to identify a wide range of taxa in a variety of environments, including but not limited to birds [31], mammals [32], and amphibians [33] using a variety of methods such as spectrogram cross-correlation and analysis [34], machine learning [35], and classification of acoustic indices ([36, 37]). While these recognition approaches have typically been used to identify acousti-

cally active animals, the same approaches can be applied to acoustically distinct abiotic sounds [38]. Automated pattern recognition is becoming increasingly user-friendly with a variety of software packages and programs available across several analysis platforms [30].

This study aims utilize a previously documented experimental crown fire [39] as a proof of concept for the combination of fire behaviour observations and the creation of a firebrand impact time series with an event-based bioacoustic recognition algorithm. The time series of firebrand impact is then related to observed fire location to reconstruct firebrand source areas, travel distances, and the relationship to observed fire behaviour.

2. Methods

2.1. Experimental Fire Description

The acoustic analysis conducted in this study is based on the experimental boreal crown fire from May 2019 in Alberta, Canada, as documented in [39]. A 3.5 ha fire was ignited via heli-torch (in a natural stand of dense black spruce (4.5 m tall., 12,000 stems ha^{-1}) with an 72% feathermoss (primarily *Pleurozium schreberi*) surface cover. The first 50 m of the stand in the direction of fire spread was untreated, with a thinning reduction to 2,300 stems ha^{-1} implemented the remainder of the stand 50 m beyond the ignition line (Fig. 1). The equilibrium rate of spread of approximately 50 m min^{-1} consumed 1.5 kg m^2 of fine fuel in the flaming phase, producing on the order of 6,900 MW of combustion energy over a flaming front 300 m wide and approximately 35 m deep. Of 11 cameras deployed, 9 were placed in the thinned area, within 20–70 m of the control. One camera (Camera 24) was located in an open area of masticated (mulched) spruce fuels to the NW, and another (Camera 25) on the edge of a 10 m wide cutline that ran southeasterly through the east thinned area. Cameras were placed strategically but unevenly across the experimental unit to capture key areas of interest for fire behaviour (e.g. transitions from unthinned to thinned; along cutlines etc.) rather than systematically. Camera placement and the experimental fire overall was conducted prior to the concept of this firebrand acoustic analysis, and hence the study was not optimized for camera firebrand acoustic monitoring, but rather to capture specifics of flaming spread and intensity, as presented in [39].

The cameras used to record video were Sony Camcorder (HDR-XR200V), recording video at AVCHD 1440 × 1080/60i format and audio in 32-bit stereo at 48 kHz. The hard disk drive recorders register a self-noise (produced by the unit itself) of approximately 40 dB(A) [40]. The cameras were contained in stainless steel boxes measuring 22.86 cm wide and 30.48 cm long, and 22.86 cm tall (only the 0.069 m^2 in top area was used in calculations). The boxes were insulated with ceramic fibreboard insulation between the steel case and the camera. Each camera is supported by three steel legs to a height of approximately 1.2 m (Figure S1).

A full exploration of the observed fire behaviour in the experimental fire is given in [39]. Litter moisture was between 9% (control) and 6.5% (thinned); spruce foliar moisture was $79 \pm 23\%$. At the time of ignition, the air temperature
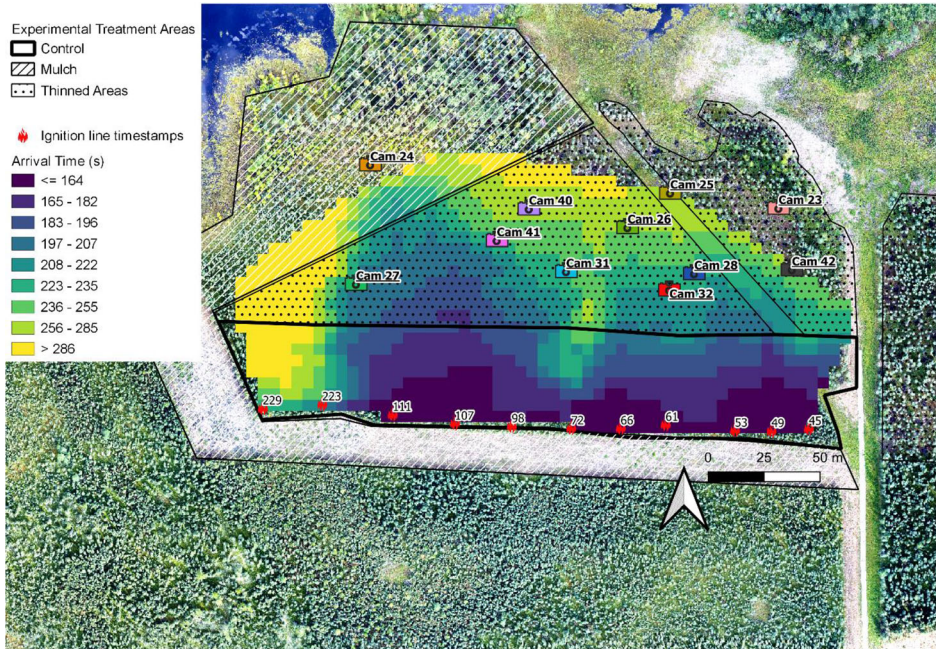
Figure 1. Camera locations and relative arrival time of the fire. A detailed description and photos of the thinning treatment and control (unthinned) areas is available in [39].

was 22.2 °C, relative humidity was 18.7%, with a mean wind speed of 12 km h^{-1} (gusting to 26 km h^{-1}). Canadian Fire Weather Index values were Fine Fuel Moisture Code 93.6, Buildup Index 69.6, and Fire Weather Index 27. In the eastern portion of the stand, the fire spread at 34 m min^{-1} through the control and 50 m min^{-1} in the treated area; spread rates in the western portion were 68 m min^{-1} in the control and 60 m min^{-1} in the treatment. Head fire intensity for the continuous crown fire in the control was calculated as 43,000 kW m^{-1} in the control and 41,000 kW m^{-1} averaged across the treatment, accounting for both canopy and surface fuels [39]. Multiple spot fires were observed and suppressed upwards of 190 m beyond the furthest extent of the thinned area. Given that there was typically only 2–3 min between ignition and the arrival of the fire front to the cameras, the in-fire video footage recorded few visible spot fires until the fire front was 20–30 m distant, at which point numerous spot fires are observed to briefly initiate before being overtaken by the main fire front (Figure S2).

Multiple spot fires were observed between 190 and 300 m beyond the furthest northern limit of the control portion of the experimental fire, where the receiving area for any firebrands consists of a mixture of cured grass leafless aspen seedlings (north of the area shown in Fig. 1). These spot fires locations were relayed by suppression resources during the experimental fire and were not recorded by any

infrared or video cameras, so the exact timing of their ignitions (and the corresponding source of the firebrand) is not known. Using the analytical firebrand travel distance model of [7] using a free flame height of 5 m (in the control), and canopy-top wind speed of 20 km h^{-1}, the modelled maximum spot fire distance is 300 m, similar to observed spot fires. A factor complicating the maximum spotting distance in the case of this experimental fire is gusty conditions and wind shear as evidenced by weak winds from the southeast at the surface interspersed with strong gusts upwards of 26 km h^{-1} from the south, which may have propelled firebrands further than mean surface wind speed measurements would have suggested. The firebrand transport distances of 10–100 m measured here did not create appreciable spot fires ahead of the main fire front, as observed from the camera footage, owing to the limited time for a surface fire to develop from a single firebrand. Longer-distance firebrands transported hundreds of metres ahead of a rapidly-moving crown fire would be sufficient to create spot fires of appreciable size prior to the arrival of the fire front [60].

2.2. *Acoustic Analysis*

Time-synchronized video from eleven cameras (Fig. 1) in an experimental crown fire in MPEG-2 Transport Stream (.m2ts) format were processed. Audio was extracted from these files and converted into 48 kHz, 16-bit depth Waveform Audio Files (.wav) for processing and recognition. The *monitoR* package [41] in R was used for automated recognition a spectrogram cross-correlation approach. The cross-correlation approach used is directly from the *monitoR* package for the acoustic detection of bird song from automated recording units placed in forest settings for the acoustic quantification of bird song occurrence and timing. As such, the *monitoR* package is designed to handle acoustic recognition of sound patterns using a moving-window cross-frequency correlation approach in settings with environmental noise such as background wind. While most bird songs are quite different and far more acoustically complex than the impact event of a firebrand against a steel box, bioacoustic recognition software has a 95% detection rate for the clicking call of the Yellow Rail (*Coturnicops noveboracensis*) that is quite similar to the acoustic signal of interest in this study [42]. The algorithm works by comparison a training audio sample, and a moving window is computed in which the training sample is compared to the audio track and a correlation score that integrates all sound frequency ranges is computed. Sound < 1 kHz was excluded due to helicopter rotor noise.

This training template matches well with the spectrogram of small branches and spruce cones dropped onto the camera body in laboratory settings (Figure S3). The training template was used to process all audio extracted from the provided camera data, resulting in a detection history output of all acoustic signals that resembled the training template. The first 25 instances of firebrands after ignition were validated on each camera by manually assessing each audio recording. Increasing cross-correlation thresholds were tested against this manually validated dataset until the optimal accuracy of 82.5% was reached at a cross-correlation threshold of 0.58 (i.e. only acoustic events exceeding a correlation of 0.58 with the

training clip were used). The same correlation threshold was used in all cameras. Detection events were recorded down to the 0.1 s interval using the software, but the detection rate was aggregated to the 10-s interval in order to match the time and space resolution of the fire progression map. All times are presented as seconds since the start of the ignition operation. Missed detections (false negatives) were more likely to occur when the amplitude of firebrands was lower or during periods of high firebrand activity and overlap, which greatly decreased the correlation score of that signal. As a result, automated recognition becomes unreliable when the environment directly at the camera is burning due to high rates of firebrand activity.

The algorithm false positive rate was determined by running the cross-correlation algorithm with the same training clip against audio collected at a subset of cameras (7 of 11) prior to any fire ignition on the day of the experiment. This pre-ignition detection rate using the same 0.58 threshold was used as the overall false positive rate in the analysis. After the fire's passage, audio recordings continued and were analyzed using the recognizer algorithm as pre-fire audio. Logically, firebrand production and impact to the camera body is extremely unlikely after the passage of the main fire front, due to the prevailing wind direction during the fire. However, acoustic detections and sound power levels were retained from post-fire acoustic detections in order to help distinguish firebrand impact acoustic events from acoustic impulse events derived from the combustion process itself [29].

2.3. Firebrand Production Rate

Two approaches were used to estimate the rate of firebrand production per unit of consumed canopy biomass (F, firebrands kg^{-1} biomass). In both cases, the firebrand receiving area used is equal only to the top of the camera boxes, as outputs from the firebrand physical transport model of Koo [3] applied to simulations of the same forest type [17] showed a dominance of the vertical velocity component upon impact to the ground surface for firebrands of intermediate distance (~ 50 m). Similarly, [19] showed that the vertical velocity component dominates the firebrand trajectory just before impact when winds are 24 km h^{-1} and travel distances are on the order of 20–50 m. Under more intense wildfire with higher lofting heights, further travel distances, and declining terminal velocity with thermal decay, this assumption no longer applies [5] In this sense, these camera boxes, despite being 3D volumes approximately 1 m above the ground, act similarly as 2D detectors as used in [23, 43] when examining medium-distance firebrand transport on the order of 10–100 m.

First, a simple method (here named "transverse uniform") assumes a uniform fuel distribution between the ignition line and the camera. A consideration is made only of the distance between the ignition line to the camera, a line that is transverse to the ignition line. This method allows for differences in fuel load at distance from the camera detector, but uniform fuel load within treatments with their long-axis orthogonal to the wind direction (Fig. 1). Average plot-level measurements of canopy fuel load (with distinct values in the control and treatment) was used. No exact knowledge of the fire's location over time is required:

$$F' = \frac{\int F(t)dt}{w_{int}A_0} \tag{1}$$

$F(t)$ is the rate of firebrand detections (number of firebrands m^2 receiving area s^{-1}) at time t, and w is the corresponding canopy fuel load (kg biomass m^{-2} source area). A_0 (m^2 source area m^{-2} receiving area) is the dispersion factor (the ratio between the source area and the receiving area). At small scales (c. 1–2 m) the value of A_0 over individual unit areas may exceed unity due to the concentration of firebrands within eddies [3]. At scales of 10–100 m, firebrand dispersion can be represented as a Gaussian dispersion transverse to the wind speed, and lognormal dispersion parallel to the wind. Accounting for both axes (transverse and parallel) from a point source of firebrands, [10] approximates firebrand dispersion from a point as an ellipse with equal major and minor axes when wind speeds are less than 5 km and a lengthening major axis (with constant minor axis) with increasing wind speed. The change in the relative size of the firebrand landing area relative to the low-wind scenario in [10] is analogous to A_0 in the above equation, and can be fitted to the form:

$$A_0 = 1 + 0.0005WS^2 \tag{2}$$

Resulting in A_0 values of 1.07 in this case study, but can increase to values greater than 2.0 if wind speeds (WS) exceed 40 km h^{-1}. The transverse uniform technique was only applied to cameras 23, 25, 26, 32, and 42 in the Thin East area, where the spread was relatively constant in direction from the ignition line to the cameras (Fig. 1). For the cameras where there are distinct fuel loads in zones transverse the direction of spread (see Fig. 1), the integrated fuel load term (w_{int}) can be weighted as:

$$w_{int} = w_c\left(\frac{d_c}{d_c + d_t}\right) + w_t\left(\frac{d_t}{d_c + d_t}\right) \tag{3}$$

where fuel load is differentiated in the control (w_c) and thinned (w_t) stands and the corresponding depth (m) of the control (d_c) and thin treated (d_t) along the axis of spread. Note that more than two zones (in addition to control and treatment) could used as Eq. 3 is expanded, but such geometry is less common in experimental fires.

A second technique leveraged the interpolation fire location over time (i.e. fire arrival time raster in 10-s timesteps at 5 m resolution) grid to reconstruct the source area of the firebrands. Assuming the local spread direction at the time of burning in the head fire is an indicator of the firebrand travel vector, the fire location raster was converted into a per-pixel spread direction using the terrain function in the R package *raster* [44]. A vector was computed at each raster cell centre, with a bearing equal to the instantaneous fire spread direction as derived from the slope of the time of arrival raster. A buffer was created around each camera location in order to estimate which locations of the active fireline were

likely to have firebrands landing at the camera location (Figure S4). The width of the buffer around the camera (Δy) was computed as the 95th percentile of the cumulative normal distribution (with mean = 0) for lateral firebrand dispersion from a point source over moderate distances (c. 30 m) as estimated by [45]:

$$\Delta y = \sqrt{2} \mathrm{erfc}^{-1} \frac{1}{10} \sigma_y \tag{4}$$

where σ_y is the standard deviation of firebrands parallel to the wind direction, and is approximated for gridded fire spread models by [45] as:

$$\sigma_y = 0.92 D \tag{5}$$

where D is the pixel width in metres. The above calculations lead to the use of a 7.4 m diameter buffer of each camera location. Vectors that intersected the buffered camera locations were retained only when the timing of the firebrand detection was within $\pm$ 20 s of the peak firebrand impact rate as shown in Table 1, and the vector origin at the fire front was recorded as a location of probable firebrand source. A total of 258 firebrand acoustic detections during the peak firebrand flux period were successfully traced back to source areas (of 6824 total acoustic detections). At each time step, a single camera can record multiple firebrand source locations. A minimum convex polygon (MCP) comprising 100% of the source area pixel locations was constructed using the *adehabitatHR* package [46] v 0.3.25 for cameras with at least five source area pixel locations. The crown fuel load raster derived from a LiDAR crown fuel model built specifically for the site [47] was sampled within bounds of the MCP. The production of firebrands per unit of crown fuel consumption using this "local maximum" approach (F', firebrands kg^{-1}) was calculated as:

$$F'_{max} = \frac{F_{max} \tau_{res}}{w_{max} A_0} \tag{6}$$

where F_{max} is the peak instantaneous recorded firebrand impact rate (number of firebrands m^{-2} receiving area s^{-1}); τ_{res} is the flaming residence time (s) of tree crown branch and foliage material as observed in the camera footage; w_{max} is the mean crown fuel load (kg m^{-2} source area) from the LiDAR fuel load grids of [47] within the MCP; and A_0 (m^2 source area m^{-2} receiving area) is the dispersion factor as defined in Eq. 2.

3. Results

Prior to the ignition of the crown fire by the heli-torch, each camera was deployed and recorded for upwards of 75 min. During those 75 min of confirmed no-fire environment, 6 of the 7 pre-fire recordings analyzed showed a low rate of false positive detections (Fig. 2), averaging 0.2 false positive detection every minute per camera. Camera 24, the sole camera in the open and not in a forest canopy,

Table 1
Summary Table of Camera Attributes and Acoustic Detection Derivatives

Camera	23	24	25	26	27	28	31	32	40	42	Avg
Distance to ignition line (m)	107	118	109	92	60	74	71	67	100	79	88
Tree density near camera†	8	0	5	27	13	13	15	18	26	26	15
Pre-ignition detection rate (impacts per camera min^{-1})	–	2.51	0.07	0.15	0.28	–	0.16	0.04	0.53	–	0.5
Ignition time‡ (s)	45	111	61	66	111	53	72	61	98	45	72
Time of peak impact rate (s)	200	230	190	180	200	180	160	190	140	200	187
Fire arrival time (s)	280	280	280	255	215	220	230	220	260	245	248
τ_{res} (s)	10	–	15	21	13	12	12	–	13	–	14
Peak impact rate (impacts per camera s^{-1})	7.3	8.8	7.5	6.1	4.4	7.7	7	3.9	2	4.3	5.9
F_{max} (impacts m^{-2} s^{-1})	105	126	108	88	63	111	100	56	29	62	85
Total detections (per camera)	499	482	373	410	288	369	526	186	73	236	344
Total detections (per m^2)	7162	6918	5353	5884	4133	5296	7549	2669	1048	3387	4939
w_{int} (kg)	100	107	102	91	71	80	78	76	96	83	88
w_{max} (kg m^{-2})	1.8	1.9	2.1	1.5	1.7	–	–	2.3	–	1.8	1.9
Camera distance to MCP centroid (m)	60	60	75	70	< 5	–	75	33	–	42	53
F' transverse uniform method (firebrands kg^{-1})	71	–	53	65	–	–	-	35	–	41	55
F'_{max} local maximum specific flux (firebrands kg^{-1})	545	867	720	1151	450	–	–	318	–	450	643
Camera	23	24	25	26	27	28	31	32	40	42	Avg

†Tree density near each camera was calculated as a sum of large trees visible from the UAV aerial imagery mosaic within a 10-m radius of each camera, including only trees from a SE to SW azimuth from each camera, or an area of 78 m^2 (135–225 degrees from true north). ‡ Ignition times refers to the timing of the ignition due south (upwind) of the camera (see Fig. 1). Camera 41 is not included due to malfunction of the camera during the firebrand impact recording period

recorded a higher rate of 2.5 false positive detections per minute, likely due to higher wind speeds rocking the camera body and causing incidental noise. Given the 6-min period between fireline ignition and passage of the fire front through all cameras, the false positive rate is at worst 2.4% for camera 24 and likely on the order of 0.25% for all other cameras. This value is far smaller than the estimated 18% false negative rate of missed detections.

The sum of detections per camera varied from 526 at camera 31 located 100 m north (downwind) of the initial ignition location, to as little as 73 at camera 40, which experienced a moderate-intensity flanking fire at the camera site. Peak rates of firebrand impacts detected on the cameras occurred when the fire was on
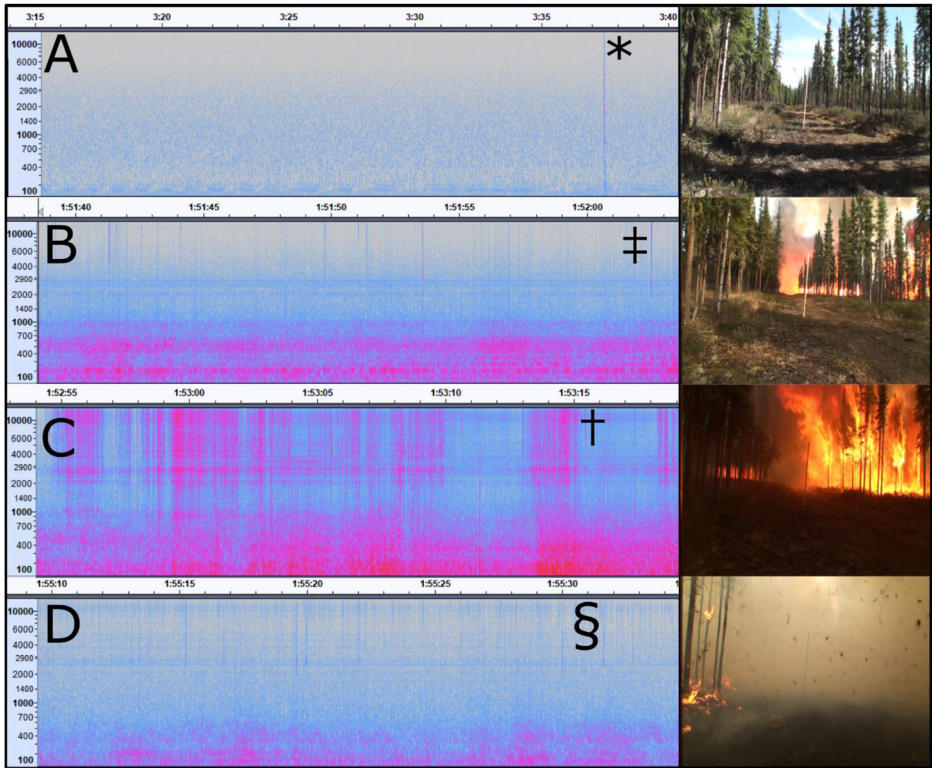
Figure 2. Spectrograms and associated video records for Camera 25, looking southeasterly along a pre-existing fuel break and access road. Timestamps in each of the four panels corresponds to time since deployment of camera, with fire ignition at approximately 1:50:00 in this camera footage. The y-axis of each panel sonogram is frequency in Hz. The * symbol in Panel A denotes a pre-ignition false positive detection. ‡ in Panel B denotes a distinct firebrand detection; † in Panel C is the onset of large numbers of firebrands that are indistinguishable and at close range to the head fire. Panel D is immediately after the fire with likely Acoustic Impulsive Events evident as noted by §.

average 50 m from the fire front (Table 1; Fig. 3). Note that the transition to a state of continuous firebrand impact from short-distance (10–20 m from fire front) saturated the acoustic recognizer algorithm, and are thus not included in this total. Peak impact rates averaged 85 impacts m^2 s^{-1} across the ten cameras that recorded impacts within 75 m of the fire's proximity. The pattern of firebrand impact as a function of distance varied greatly, with a number of cameras reporting unimodal responses with a maximum at distance (camera 25), or at closer ranges (camera 42). Bimodal patterns were seen (cameras 24 and 26) as well as monotonic ones (cameras 27 and 40). Despite the variety of camera locations
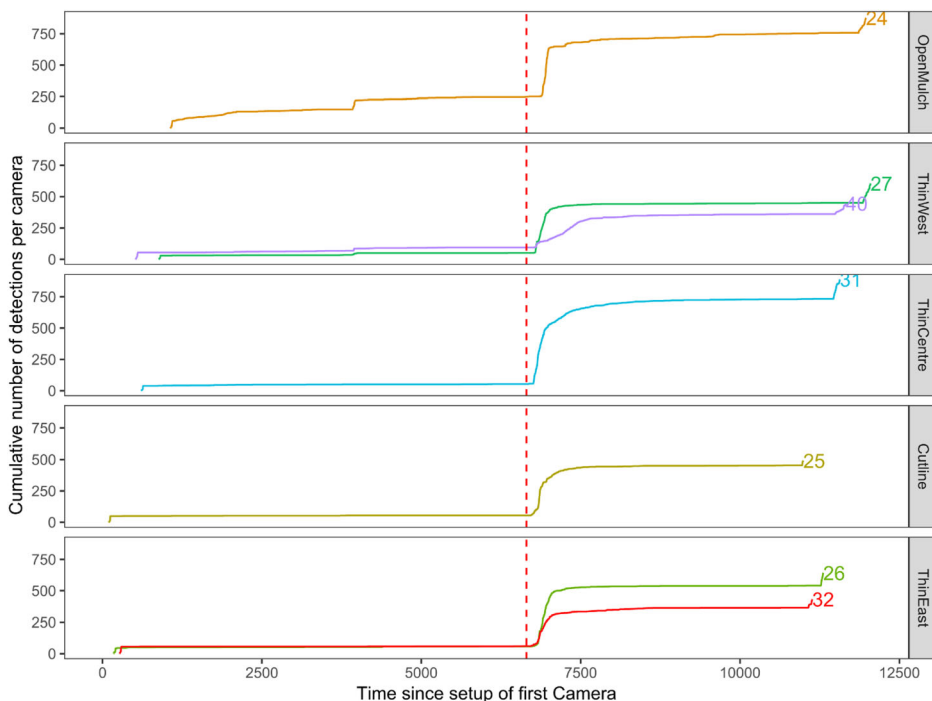
Figure 3. Cumulative firebrand detections (with a correlation score greater than 0.58). The origin of the x-axis corresponds to the setup of the first camera approximately 110 min prior to ignition. The red vertical dashed line shows the ignition time. Detections to the left of the dashed red line correspond to false positive detections. Acoustic detections after the passage of the fire front (approximately time step 7,000) are shown here, but not otherwise included in the analyses.

relative to the control and ignition line, the vast majority of cameras reported a fire location at the time of peak firebrand production within the control (Fig. 4), except in the case of cameras such as 24 and 27 where the camera location was never directly downwind of the main fire front, and instead only experienced the peak firebrand impact rate when a flanking (lateral spread) fire approached on a WNW vector. An inverse relationship was observed between canopy density and the peak firebrand impact rates (Spearman's correlation coefficient $\rho = -0.77$; see Table S1) as well as between canopy density and total number of detections ($\rho = -0.44$) suggesting some role of overstory trees in intercepting the firebrands detected by the camera acoustic signatures is possible.

For the transverse uniform scheme averaged across the entire source area from the ignition line to the camera (Eq. 1), the number of firebrands detected as a function of total fuel consumed was on average 59 firebrands kg^{-1} when only canopy fine fuels (foliage, arboreal lichens, and fine branchwood < 1 cm) are considered. Since the assumption of linear spread of a head fire was only satisfied for
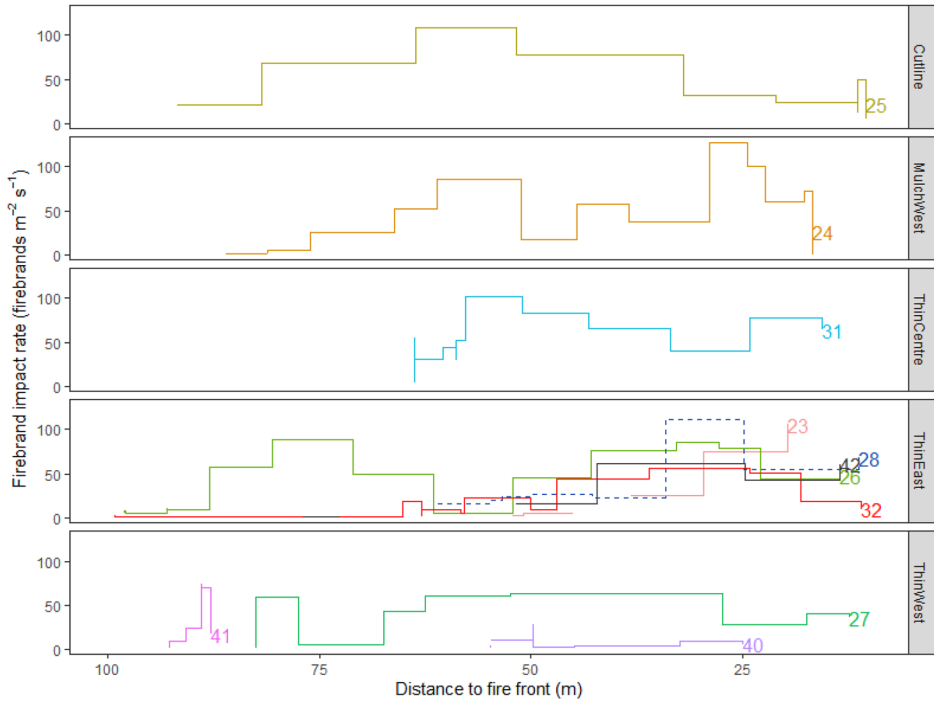
Figure 4. Firebrand impact rate (10-s moving window average) as a function of distance to the fire front.

cameras in the eastern thinned area, only those cameras have a firebrand production rate shown in Table 1. The source area inference method from the instantaneous spread direction (Eq. 6) yielded higher estimated production values, with a median value of 643 firebrands kg^{-1} across the seven cameras where the source area calculation was possible. This second method yielded a variability in the production estimates from 318 (Camera 32) to 1151 (Camera 26) firebrands kg^{-1}. With firebrand production estimates from the instantaneous maximum approach approximately 11 times higher than the averaging/integration approach, this suggests that the peak firebrand pulse represents on the order of 90% of the total firebrand input prior to the fire's arrival.

4. Discussion

An average of 4,900 firebrands were detected per m^2 by cameras in this study in the time between fire ignition at the arrival of the fire front. This compares to the approximately 1,500 firebrands per m^2 detection rate in controlled outdoor ignitions of between 1 and 5 trees [48]. Field studies of incidental detections such as in trampolines [23] for a lower-intensity fire in a pine stand, found total firebrand impact densities of 330–530 firebrands m^{-2}, with peak impact rates of 0.8–1.0 fire-

brands m^2 s^{-1}. The study of [23] used video recordings of aluminum tins adjacent to but not in the direct path of an experimental fire. The impact of the lower fire intensity (only 25% of that in this study) and large contrasts in tree physiology and structure between spruce and pine prevents the direct comparison of results, but broadly corresponds to the expected non-linear increase in firebrand production and travel with increasing fireline intensity.

The analytical firebrand model of [19] predicts transport distances that are similar to those observed in this study. Using a 5 mm diameter and 15 mm length cylinder under 25 km h^{-1} wind, a mean transport distance of 40 m is predicted in [19], similar to the mean distance from camera to the centroid of the firebrand MCP of 50 m observed in this study. With a mean firebrand mass of approximately 0.15 g, the $\sim$ 640 firebrands kg^{-1} documented in this experimental crown fire would yield around 90 g of firebrand material per kg of total crown fuel (foliage biomass plus fine branchwood). This firebrand yield is higher than the 2–20 g firebrands kg^{-1} crown consumption as summarized in laboratory experimental consumption of single conifer trees in [8]. Using the lower production rates from the transverse uniform method (Eq. 1), total estimated firebrand mass would be more on the order of 8 g kg^{-1}, similar than the range presented in [8]. Although the new methodology presented here requires further cross-validation with other methods, the number of firebrands detected and the distance from the fire are in the ranges from modelling, laboratory, and the limited set of outdoor experimental fires.

In addition to the distinct firebrand impact events recorded in the camera audio track, numerous other acoustic phenomenon were recorded. Strong ambient winds are typical of high-intensity wildfires, as are fire-induced winds both before the arrival of the fire front (indraft) as well as after [49]. While ambient wind speeds were relatively light on the day of the experimental fire (12 km h^{-1} gusting to 26 km h^{-1}) the stronger fire-induced winds created noticeable sound in the camera recording, as captured by the Normalized Difference Soundscape Index [50] (Suppl. Figure S5). NDSI values of -0.5 to 0.0 at ignition increased to 0.5 to 0.9 at the time of fire passage, and remained elevated for 400–600 s after ignition. Alongside this fire-induced wind was episodic sounds similar to the firebrand impact, but occurring exclusively after the passage of the fire front when the fire had passed and no further high-intensity fire was upwind. These events and those observed during the active flaming observations at each camera likely correspond to the combustion-derived Acoustic Impulsive Events (AIE) [29]. Such AIE as recorded by [29] had an a sound pressure of 2 Pa recorded at 0.25 m distance, equivalent to 60 dB at 0.25 m measurement distance. Similar AIE produced at the main flaming fire front but recorded 25 m away, coincident with the shortest distance of maximum firebrand production for most cameras (Fig. 3), would register at 20 dB. This 20 dB noise would be far below the approximately 40 dB hard drive noise of the camera units [40]. Such low sound intensities of AIEs would only be recorded by these camera units if within 2.5–3.0 m of the fire front, assuming an ideal inverse-square decay in sound intensity with distance. For these high-intensity wildfires, numerous visible firebrands alongside strong indraft winds are apparent in the camera footage that likely inhibit the detection of AIEs. For

lower-intensity surface fires with fewer firebrands [3] and using more specialized acoustic equipment, AIEs would need to be distinguished from firebrand impact events. The rate and intensity of AIEs may be related to combustion rates of duff and other thermally thick materials immediately after the passage of the main flaming front. This transitional consumption period of high soil heat inputs from the flaming front is only broadly understood [51] but is an important link between in-fire heat transfer processes and smouldering consumption models that largely exclude the consumption processes of the uppermost duff or peat horizons [52]. Future studies could examine the acoustic patterns during and immediately after the passage of the fire front using the same footage as this study, particularly if paired with infrared imagery that captures smouldering consumption rates [53].

The pre-ignition detection rate of 0.5 false positives per camera minute in small in contrast to the c. 350 total detections per camera during the experimental fire (Table 1). This suggests the false positive rate is on the order of 1.0–1.5% of total detections. The source of the false positives was not concretely examined, but a likely source of false positives include the camera leg retention pins striking the camera body when exposed to wind. High false positive detections were noted in Camera 24, which sat in an open area and was exposed to far more wind than any other camera. Future deployments of this equipment will secure these retention pins in order to further reduce the false positive rate. Some false positives may also be due to the numerous large biting flies of the family Tabanidae that are common in the region and attracted to dark coloured cubes: in this case, a soot-covered camera box [54]. The authors routinely observe flies of this family flying into metal objects with force; given the fly's size of c. 300 mg [55], this too may result in false positive detections. Flies of this variety are routinely controlled using dark metal spheres to lure them away from livestock [56].

The firebrand densities documented in this study are not necessarily reflective of firebrands with sufficient thermal energy to ignite materials, which have been incidentally documented in partially ignited materials [22] or through thermal imaging [2, 57]. This technique has the advantage of utilizing existing experimental fire equipment, using a simple, existing acoustic analysis technique that can be applied to historical in-fire camera footage for added value to existing experimental fire documentation. However, the fraction of firebrands as detected by this acoustic technique that have sufficient heat content to lead to the ignition of surface fuels is unknown. Observations in a controlled outdoor setting of ember generation and heat content [43] suggest that between 6 and 30% of firebrands are of sufficient temperature and size to sustain ignition over distances as far as 8 m.

The distance of the maximum instantaneous firebrand impact rates observed here, often peaking between 10 to 90 m from the fire front (excluding the very close-range ember shower of < 10 m within a head fire) coincides with previous studies on the efficacy of fuel breaks. For wildfires in western USA, typically of lower intensity than the experimental fire studied here, roadways and mechanically cleared (bulldozer with blade) fuel breaks both on the order of 10 m wide were effective in stopping fire spread only 50% of the time [58]. Storey et al. [2], in their analysis of spot fires in Australia that were closer to the fireline intensity observed here, showed a median spot fire distance of 100 m. In Canada, the zone

30–100 m from homes is considered the outermost "zone 3" where thinning and pruning treatments are recommended to reduce individual tree torching [59]; tree torching and crown consumption creates updrafts that are conducive to firebrand generation and travel [3].

All but two cameras 24 and 27 showed a peak firebrand production rate in the control (Fig. 5). Wildfire physics modelling using FIRETEC to simulate fire behaviour and firebrand transport and production was conducted in this same fuel complex [17] using a constant firebrand production rate per unit volume of canopy, but limiting firebrand transport by a minimum vertical updraft velocity criteria at launch. Solely by the reduction in intensity due to thinning of dense clusters of black spruce, firebrand production was estimated to be reduced by approximately 75% [17]. Direct comparisons are difficult due to the conflation of distance to the camera and fuel load (i.e. the cameras in this study were placed in the thinned treatment). However, the pattern of 8 of 10 cameras observing a source area for the peak firebrand shower in the denser control area suggests a bias towards increased firebrand production and transport in the control. Flame length observations indicate double the flame height and threefold higher intensity in the control as compared to the treatment [39].

Though the proof of concept shown here only applies to a single experimental fire, the methodology used may be applied to archival footage of well-documented experimental fires [57, 61, 62] in order to compute a larger number of firebrand production values across a variety of fuel and fire intensity settings. The firebrand production and travel estimates produced from this method may also be used to improve parameter estimates for firebrand transport models [3, 18]. Future extension of this method will involve the analysis of the amplitude of the firebrand impact event, as it likely relates to the kinetic energy of the impacting firebrand. Similar techniques are used in the measurement of rain drop kinetic energy with acoustic distrometers [63].

5. Conclusion

A well-observed experimental crown fire in a Canadian boreal spruce stand was analyzed for the acoustic detection of firebrands impact in-fire camera boxes. Firebrand detections were detected with low false negative rate ($< 15\%$) and very low false positive rate ($< 1\%$). The methodology documented here represents an opportunity to re-examine prior experimental fires to compute firebrand production rates where two key datasets are available: (1) preserved audio tracks of in-fire cameras; (2) well-documented rate of spread over time, via a dense rate of spread timer grid, or else reconstructed from aerial video. Firebrand impacts were detected up to 100 m away, with a rapid increase in the detection rate around 75 m. Using a spatial estimate for the consumption of canopy fuels, it is estimated that 640 firebrands were detected per kg of canopy fuel consumed, when considering only the peak medium-distance firebrand shower approximately 50 m from the fire front. This peak coincided with the highest observed fireline intensity values in the unthinned area. This strong pattern of firebrand production in the control
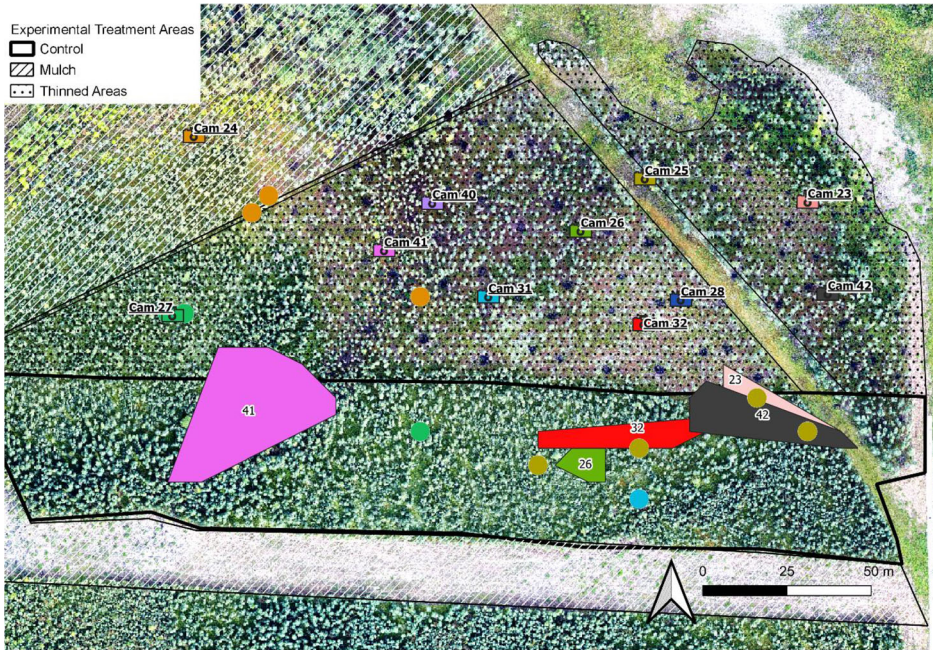
Figure 5. Reconstruction of peak firebrand impact source area. Only firebrands within ± 20 s of the peak firebrand impact rate for each camera are shown. Symbols show camera location, and polygon of corresponding colour shows minimum convex polygon of firebrand source area. Where < 5 source areas prevented the calculation of an MCP individual source area points are shown as coloured circles.

with two to three-fold higher fire intensity suggests this observed fire front distance at peak firebrand shower may be farther than in a scenario of uniform fuels. The observed bias towards enhanced firebrand production and transport in pockets of high intensity fire corresponds with analytical firebrand models as well as fire fluid dynamics models. Observations here also corroborate community wildfire mitigation guidance that emphasizes the reduction in tree torching potential (and therefore intensity) in the 30 to 100 m from structures as a key method of reducing the firebrand influx.

Acknowledgements

Author's contributions

Conceptualization, DT and DY: Methodology, DY, DT, GM: Validation, DT, DY: Formal Analysis, DT, EK, RL: Investigation, RR: Resources, DS: Data Curation, DT: Writing—Original Draft Preparation, all; Writing—Review and Editing, all; Visualization, DT: Supervision, DT: Project Administration, DT: All authors read and approved the final manuscript.FundingAlberta Wildfire Management Branch provided the resources to conduct the experimental fire.

Declarations

Conflict of interest   The authors declared that there is no conflict of interest.

Data availability   The datasets generated during and/or analysed during the current study are available in the Zenodo repository, https://doi.org/10.5281/zenodo.3746895

Code availability   The R script used to conduct the above analysis is also available via the same Zenodo repository, https://doi.org/10.5281/zenodo.3746895

Open Access

References

1. Cohen JD (2000) Preventing disaster: home ignitability in the wildland-urban interface. J For 98:15–21. https://doi.org/10.1093/jof/98.3.15
2. Storey MA, Price OF, Sharples JJ, Bradstock RA (2020) Drivers of long-distance spotting during wildfires in south-eastern Australia. Int J Wildland Fire 29:459–472. https://doi.org/10.1071/WF19124
3. Koo E, Linn RR, Pagni PJ, Edminster CB (2012) Modelling firebrand transport in wildfires using HIGRAD/FIRETEC. Int J Wildland Fire 21:396–417. https://doi.org/10.1071/WF09146
4. Beverly JL, Wotton BM (2007) Modelling the probability of sustained flaming: predictive value of fire weather index components compared with observations of site weather

and fuel moisture conditions. Int J Wildland Fire 16:161–173. https://doi.org/10.1071/WF06072

5. Tarifa CS, del Notario PP, Moreno FG (1965) On the flight paths and lifetimes of burning particles of wood. Symp Int Combust 10:1021–1037. https://doi.org/10.1016/S0082-0784(65)80244-2

6. Albini FA (1979) Spot fire distance from burning trees: a predictive model. intermountain forest and range experiment station, Forest Service, U.S. Dept. of Agriculture, Ogden, Utah

7. Albini FA, Alexander ME, Cruz MG (2012) A mathematical model for predicting the maximum potential spotting distance from a crown fire. Int J Wildland Fire 21:609–627. https://doi.org/10.1071/WF11020

8. Manzello SL, Suzuki S, Gollner MJ, Fernandez-Pello AC (2020) Role of firebrand combustion in large outdoor fire spread. Prog Energy Combust Sci 76:100801. https://doi.org/10.1016/j.pecs.2019.100801

9. Waterman TE (1969) Experimental study of firebrand generation. office of civil defense, office of the secretary of the army, Washington, DC

10. Zhao S (2011) Simulation of mass fire-spread in urban densely built areas based on irregular coarse cellular automata. Fire Technol 47:721–749. https://doi.org/10.1007/s10694-010-0187-4

11. Suzuki S, Manzello SL, Lage M et al (2012) Firebrand generation data obtained from a full-scale structure burn. Int J Wildland Fire 21:961–968. https://doi.org/10.1071/WF11133

12. Suzuki S, Manzello SL (2016) Firebrand production from building components fitted with siding treatments. Fire Saf J 80:64–70. https://doi.org/10.1016/j.firesaf.2016.01.004

13. Manzello SL, Suzuki S, Naruse T (2019) Quantifying wind-driven firebrand production from roofing assembly combustion. Fire Mater 43:3–7. https://doi.org/10.1002/fam.2661

14. Masoudvaziri N, Bardales FS, Keskin OK et al (2021) Streamlined wildland-urban interface fire tracing (SWUIFT): modeling wildfire spread in communities. Environ Model Softw . https://doi.org/10.1016/j.envsoft.2021.105097

15. Alexander ME, Stefner CN, Mason JA, et al (2004) Characterizing the jack pine-black spruce fuel complex of the International Crown Fire Modelling Experiment (ICFME). Canadian Forest Service, Edmonton, Canada

16. Canfield JM, Linn RR, Sauer JA et al (2014) A numerical investigation of the interplay between fireline length, geometry, and rate of spread. Agric For Meteorol 189–190:48–59. https://doi.org/10.1016/j.agrformet.2014.01.007

17. Marshall G, Thompson DK, Anderson K et al (2020) The impact of fuel treatments on wildfire behavior in North America Boreal fuels: a simulation study using FIRETEC. Fire 3:18. https://doi.org/10.3390/fire3020018

18. Martin J, Hillen T (2016) The spotting distribution of wildfires. Appl Sci 6:177. https://doi.org/10.3390/app6060177

19. Anthenien RA, Tse SD, Carlos Fernandez-Pello A (2006) On the trajectories of embers initially elevated or lofted by small scale ground fire plumes in high winds. Fire Saf J 41:349–363. https://doi.org/10.1016/j.firesaf.2006.01.005

20. Hudson TR, Blunck DL (2020) Effects of fuel characteristics on ember generation characteristics at branch-scales. Int J Wildland Fire 28:941–950. https://doi.org/10.1071/WF19075

21. Cruz MG, Sullivan AL, Gould JS et al (2012) Anatomy of a catastrophic wildfire: the black saturday kilmore east fire in Victoria, Australia. For Ecol Manag 284:269–285. https://doi.org/10.1016/j.foreco.2012.02.035

22. Manzello SL, Foote EID (2014) Characterizing firebrand exposure from wildland-urban interface (WUI) fires: results from the 2007 angora fire. Fire Technol 50:105–124. https://doi.org/10.1007/s10694-012-0295-4

23. Thomas JC, Mueller EV, Santamaria S et al (2017) Investigation of firebrand generation from an experimental fire: development of a reliable data collection methodology. Fire Saf J 91:864–871. https://doi.org/10.1016/j.firesaf.2017.04.002

24. Storey MA, Price OF, Bradstock RA, Sharples JJ (2020) Analysis of variation in distance, number, and distribution of spotting in Southeast Australian wildfires. Fire 3:10. https://doi.org/10.3390/fire3020010

25. Manzello SL, Suzuki S, Hayashi Y (2012) Exposing siding treatments, walls fitted with eaves, and glazing assemblies to firebrand showers. Fire Saf J 50:25–34. https://doi.org/10.1016/j.firesaf.2012.01.006

26. Bouvet N, Link ED, Fink SA (2020) Development of a new approach to characterize firebrand showers during Wildland-Urban Interface (WUI) fires: a step towards high-fidelity measurements in three dimensions. National Institute of Standards and Technology, Gaithersburg, MD

27. Krautz J (1997) Appendix C-insulated boxes for protecting video cameras. In: Mangan R (ed) Surviving fire entrapments comparing conditions inside vehicles and fire shelters, 9751–2817-MTDC. Missoula, MT, pp 39–40

28. Taylor SW, Wotton BM, Alexander ME, Dalrymple GN (2004) Variation in wind and crown fire behaviour in a northern jack pine-black spruce forest. Can J For Res 34:1561–1576. https://doi.org/10.1139/x04-116

29. Yedinak KM, Anderson MJ, Apostol KG, Smith AMS (2017) Vegetation effects on impulsive events in the acoustic signature of fires. J Acoust Soc Am 141:557–562. https://doi.org/10.1121/1.4974199

30. Knight E, Hannah K, Foley G et al (2017) Recommendations for acoustic recognizer performance assessment with application to five common automated signal recognition programs. Avian Conserv Ecol . https://doi.org/10.5751/ACE-01114-120214

31. Pérez-Granados C, Bota G, Giralt D, Traba J (2018) A cost-effective protocol for monitoring birds using autonomous recording units: a case study with a night-time singing passerine. Bird Study 65:338–345. https://doi.org/10.1080/00063657.2018.1511682

32. Garland L, Crosby A, Hedley R et al (2020) Acoustic versus photographic monitoring of gray wolves (Canis lupus): a methodological comparison of two passive monitoring techniques. Can J Zool . https://doi.org/10.1139/cjz-2019-0081

33. Annich N, Bayne E, Paszkowski C (2019) Identifying Canadian toad (Anaxyrus hemiophrys) habitat in northeastern Alberta, Canada. Herpetol Conserv Biol 14:503–514

34. Clark CW, Marler P, Beeman K (1987) Quantitative analysis of animal vocal phonology: an application to swamp sparrow song. Ethology 76:101–115. https://doi.org/10.1111/j.1439-0310.1987.tb00676.x

35. Thakur A, Thapar D, Rajan P, Nigam A (2019) Deep metric learning for bioacoustic classification: overcoming training data scarcity using dynamic triplet loss. J Acoust Soc Am 146:534–547. https://doi.org/10.1121/1.5118245

36. Phillips YF, Towsey M, Roe P (2018) Revealing the ecological content of long-duration audio-recordings of the environment through clustering and visualisation. PLoS ONE 13:e0193345. https://doi.org/10.1371/journal.pone.0193345

37. Yip DA, Mahon CL, MacPhail AG, Bayne EM (2021) Automated classification of avian vocal activity using acoustic indices in regional and heterogeneous datasets. Methods Ecol Evol n/a: . https://doi.org/10.1111/2041-210X.13548

38. Chung KW, Sutin A, Sedunov A, Bruno M (2010) Cross-correlation method for measuring ship acoustic signatures. Proc Meet Acoust 11:055002. https://doi.org/10.1121/1.3559152

39. Thompson DK, Schroeder D, Wilkinson SL et al (2020) Recent crown thinning in a boreal black spruce forest does not reduce spread rate nor total fuel consumption: results from an experimental crown fire in Alberta, Canada. Fire 3:28. https://doi.org/10.3390/fire3030028

40. Gao F, Lin W, Sundaradivelu K et al (2009) Airflow-induced noise and prediction for high-spinning-speed hard disk drive. Mech Based Des Struct Mach 37:413–429. https://doi.org/10.1080/15397730903008382

41. Katz J, Hafner SD, Donovan T (2016) Tools for automated acoustic monitoring within the R package monitoR. Bioacoustics 25:197–210. https://doi.org/10.1080/09524622.2016.1138415

42. Sidie-Slettedahl AM, Jensen KC, Johnson RR et al (2015) Evaluation of autonomous recording units for detecting 3 species of secretive marsh birds. Wildl Soc Bull 39:626–634. https://doi.org/10.1002/wsb.569

43. Adusumilli S, Hudson T, Gardner N, Blunck DL (2020) Quantifying production of hot firebrands using a fire-resistant fabric. Int J Wildland Fire . https://doi.org/10.1071/WF20051

44. Hijmans RJ, Etten J van, Sumner M, et al (2020) Raster: geographic data analysis and modeling

45. Himoto K, Tanaka T (2008) Development and validation of a physics-based urban fire spread model. Fire Saf J 43:477–494. https://doi.org/10.1016/j.firesaf.2007.12.008

46. Calenge C, Royer contributions from SD and M (2020) adehabitatLT: analysis of animal movements

47. Cameron H (2020) Predicting fuel characteristics of black spruce stands using airborne laser scanning (ALS) in the Province of Alberta, Canada. In: ERA. https://era.library.ualberta.ca/items/780d87fb-38de-4d4b-910d-0afd159a1cab. Accessed 1 Dec 2020

48. Hudson TR, Bray RB, Blunck DL et al (2020) Effects of fuel morphology on ember generation characteristics at the tree scale. Int J Wildland Fire . https://doi.org/10.1071/WF19182

49. Dupuy J-L, Linn RR, Konovalov V et al (2011) Exploring three-dimensional coupled fire–atmosphere interactions downwind of wind-driven surface fires and their influence on backfires using the HIGRAD-FIRETEC model. Int J Wildland Fire 20:734–750. https://doi.org/10.1071/WF10035

50. Kasten EP, Gage SH, Fox J, Joo W (2012) The remote environmental assessment laboratory's acoustic library: an archive for studying soundscape ecology. Ecol Inform 12:50–67. https://doi.org/10.1016/j.ecoinf.2012.08.001

51. Thompson DK, Wotton BM, Waddington JM (2015) Estimating the heat transfer to an organic soil surface during crown fire. Int J Wildland Fire 24:120–129. https://doi.org/10.1071/WF12121

52. Huang X, Rein G (2017) Downward spread of smouldering peat fire: the role of moisture, density and oxygen supply. Int J Wildland Fire 26:907–918. https://doi.org/10.1071/WF16198

53. Prat-Guitart N, Rein G, Hadden RM et al (2016) Propagation probability and spread rates of self-sustained smouldering fires under controlled moisture content and bulk density conditions. Int J Wildland Fire 25:456–465. https://doi.org/10.1071/WF15103

54. Bracken GK, Wm H, Thorsteinson AJ (1962) The orientation of horse flies and deer flies (tabanidae:diptera): ii. the role of some visual factors in the attractiveness of decoy silhouettes. Can J Zool 40:685–695. https://doi.org/10.1139/z62-064

55. Belyaev OA, Farisenkov SE (2019) A study on allometry of wing shape and venation in insects. part 2. Diptera Mosc Univ Biol Sci Bull 74:7–14. https://doi.org/10.3103/S0096392519010024

56. Thorsteinson AJ, Bracken GK, Hanec W (1964) The manitoba horse fly trap. Can Entomol 96:166–166. https://doi.org/10.4039/Ent96166-1

57. Coen J, Mahalingam S, Daily J (2004) Infrared imagery of crown-fire dynamics during FROSTFIRE. J Appl Meteorol 1988–2005(43):1241–1259

58. Gannon BM, Wei Y, Thompson MP (2020) Mitigating source water risks with improved wildfire containment. Fire 3:45. https://doi.org/10.3390/fire3030045

59. FireSmart Canada (2003) FireSmart: protecting your community from wildfire. Second Edition. FireSmart Canada

60. Alexander ME, Cruz MG (2006) Evaluating a model for predicting active crown fire rate of spread using wildfire observations. Can J For Res 36:3015–3028. https://doi.org/10.1139/x06-174

61. Linn R, Anderson K, Winterkamp J et al (2012) Incorporating field wind data into FIRETEC simulations of the International Crown Fire Modeling Experiment (ICFME): preliminary lessons learned. Can J For Res 42:879–898. https://doi.org/10.1139/x2012-038

62. Gould JS, Scion (Organization: N.Z.), Project Vesta, et al (2007) Project Vesta: Fire in dry eucalypt forest: fuel structure, fuel dynamics and fire behaviour. CSIRO PUBLISHING, Canberra, ACT

63. Winder P, Paulson KS (2011) The measurement of rain kinetic energy and rain intensity using an acoustic disdrometer. Meas Sci Technol 23:015801. https://doi.org/10.1088/0957-0233/23/1/015801